

**LEVEL**

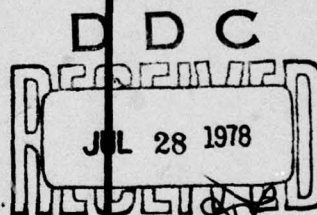
12  
SC

**Technical Report**

**526**

**K. L. Wang**

**Modal Analysis  
of SAW Convolver**



**13 January 1978**

Prepared for the Defense Advanced Research Projects Agency  
under Electronic Systems Division Contract F19628-78-C-0002 by

**Lincoln Laboratory**

MASSACHUSETTS INSTITUTE OF TECHNOLOGY

LEXINGTON, MASSACHUSETTS



Approved for public release; distribution unlimited.

78 07 24 043

AD No. \_\_\_\_\_  
DDC FILE COPY

AD A 056809

The work reported in this document was performed at Lincoln Laboratory, a center for research operated by Massachusetts Institute of Technology. This work was sponsored by the Defense Advanced Research Projects Agency under Air Force Contract F19628-78-C-0002 (ARPA Order 2929).

This report may be reproduced to satisfy needs of U.S. Government agencies.

The views and conclusions contained in this document are those of the contractor and should not be interpreted as necessarily representing the official policies, either expressed or implied, of the United States Government.

This technical report has been reviewed and is approved for publication.

FOR THE COMMANDER

*Raymond L. Loiselle*

Raymond L. Loiselle, Lt. Col., USAF  
Chief, ESD Lincoln Laboratory Project Office

Non-Lincoln Recipients

**PLEASE DO NOT RETURN**

Permission is given to destroy this document  
when it is no longer needed.

12

MASSACHUSETTS INSTITUTE OF TECHNOLOGY  
LINCOLN LABORATORY

6 MODAL ANALYSIS OF SAW CONVOLVER ,

10 Karl L. WANG, Consultant  
Group 86

DDC  
JUL 28 1978  
F

9 TECHNICAL REPORT 526

14 TR-526

11 13 JAN 1978

12 HOP.

18 ESD

15 Approved for public release; distribution unlimited.  
F19628-78-C-dφφ2,  
ARPA order-2929

19 78-3

LEXINGTON

MASSACHUSETTS

207650



# ABSTRACT

The gap-coupled acoustoelectric convolver developed at Lincoln Laboratory is a surface-acoustic-wave (SAW) device consisting of a  $\text{LiNbO}_3$  delay line and a silicon strip supported on a series of spacer rails (or posts) which have been ion-beam etched into the  $\text{LiNbO}_3$  surface. The silicon/air-gap/ $\text{LiNbO}_3$  structure forms an over-moded acoustic waveguide. A theoretical model has been developed which analyzes the perturbing effect of rails and predicts the mode structure and beating phenomena between modes. The scattering by support posts is also analyzed.

ACCESSION for	
NTIS	White Section <input checked="" type="checkbox"/>
DDC	Buff Section <input type="checkbox"/>
UNANNOUNCED	<input type="checkbox"/>
JUSTIFICATION	
BY	
DISTRIBUTION/AVAILABILITY CODES	
Dis	SPECIAL
A	



## CONTENTS

Abstract	iii
I. INTRODUCTION	1
II. REVIEW OF PERIODIC TRANSMISSION LINE	3
A. Scattering Matrix	3
B. Periodic Structure	5
III. QUALITATIVE DESCRIPTION OF THE MODES	7
IV. SCATTERING MATRIX REPRESENTATION OF THE RAIL STRUCTURE	9
A. Green's Function of a Point Source	10
B. Static Green's Function of a Point Source	13
C. Green's Function of a Modulated Line Source	13
D. Stiffness Matrix	15
E. Reaction of Scattered Wave on the Source	15
F. Dynamic Equation of the Rail Structure	16
G. Scattering Matrix of the Rail Structure	17
H. Conservation of Energy	19
V. RESULTS ON THE RAIL STRUCTURE	19
A. Reflection Coefficient	19
B. Modes of the Periodic Rail Structure	21
VI. POST SCATTERING	23
A. Green's Function	24
B. Stiffness Matrix	24
C. Radiation Patterns of the Post Structure	24
VII. SUMMARY	26
References	27
APPENDIX A - Green's Function of a Modulated Line Source	29
APPENDIX B - Stiffness Tensor for the Rail Structure	31
APPENDIX C - Green's Function of a Point Source	33
APPENDIX D - Stiffness Tensor for the Post Structure	35

## MODAL ANALYSIS OF SAW CONVOLVER

### I. INTRODUCTION

In surface-acoustic-wave convolvers,<sup>1,2</sup> a semiconductor is placed in close proximity to the piezoelectric medium so that the electric field of the SAW can interact with the semiconductor to produce the desired nonlinear effect. Two types of supporting structure have been tried including<sup>3</sup> the random-post-support and the finite-periodic rail-support structure. The post support<sup>4</sup> is unsatisfactory because of the excessive loss and nonuniformity found among the devices tested. The rail structure<sup>5</sup> is a more recent development which seems to have several advantages over the random-post-support structure. Because it is a simpler and more deterministic structure, the effects of parameter variations are more controllable and suitable for analytical study.

Indeed, measurements by Reible<sup>6</sup> on the prototype rail-support device show some very interesting phenomena such as the laser-probe scan of the acoustic-field profile (Fig. 1) and the frequency response of the output (Fig. 2). A distinctive feature in these measurements is the beat characteristic. As evident from Fig. 1, the acoustic field repeats spatially in a periodic fashion. We will refer to the periodicity as the beat length. Experimentally, the beat length was measured to be approximately 137 Rayleigh wavelengths.<sup>6</sup> The output frequency response of Fig. 2 shows a frequency ripple in the order of 3 dB. The beat is the result of interference between the acoustic modes of the device which are analogous to the modes of a periodic loaded transmission line. The discontinuity presented by rail structure causes the incident Rayleigh wave to be scattered periodically in the transverse direction. This scattering process resembles the reflection of a wave in a transmission line by discrete elements spaced periodically at fixed intervals along the line.

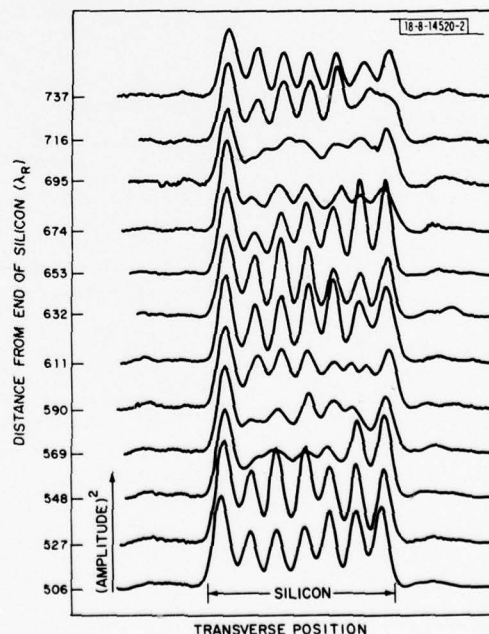


Fig. 1. Laser-probe measurement of acoustic-field profile (eight support rails).

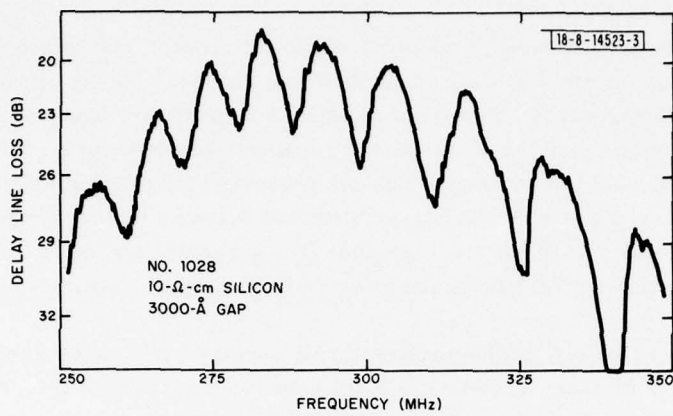


Fig. 2. Output frequency response.

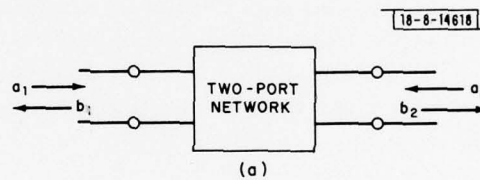
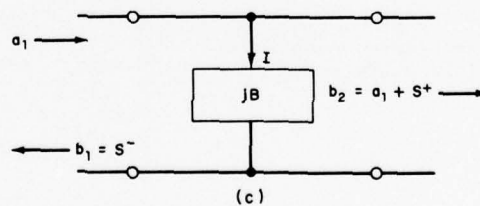
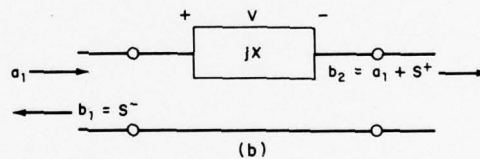


Fig. 3. Equivalent circuits in a transmission line: (a) two port, (b) series element, and (c) shunt element.





In adopting the periodic transmission line model, we have assumed first of all that the finite array of rails can be approximated by an infinite periodic structure. This seems to be a good assumption in view of the acoustic-field profile measurement which shows no changes of the envelope structure connected with edge effects of the finite transverse dimension. Secondly, the finite width of the rails is ignored by modeling them as discrete elements in a transmission line. This approximation is justified because the width is small compared with the transverse Rayleigh wavelength.

In Sec. II, we review the scattering matrix of two ports and properties of periodic structures. Section III gives a preview of the kinds of modes to be expected in the periodic rail structure by providing a qualitative description of the guided modes and their dependence on the reflection coefficient. Then in Sec. IV, we give the elastodynamics of the rail structure. The analysis of this section enables the characterization of the rail structure in terms of its scattering matrix coefficients. It is shown that the derived scattering matrix obeys the conservation of energy. Using the model developed in Sec. IV, we next study in Sec. V the reflection coefficients and the modes in the periodic rail structure as a function of the geometry of the device. Finally, in Sec. VI, the problem of Rayleigh wave scattering by the post structure is solved.

## II. REVIEW OF PERIODIC TRANSMISSION LINE

In this section, we will briefly review the scattering matrix description of two-port junctions and discuss the periodic transmission-line structure made up of a cascade connection of basic unit cells consisting of a two port and a section of transmission line.

### A. Scattering Matrix

In general, the incident- and scattered-wave amplitudes of a two-port junction shown in Fig. 3(a) are related by<sup>7</sup>

$$\begin{pmatrix} b_1 \\ b_2 \end{pmatrix} = \begin{pmatrix} S_{11} & S_{12} \\ S_{21} & S_{22} \end{pmatrix} \begin{pmatrix} a_1 \\ a_2 \end{pmatrix} \quad (1)$$

where  $a_1$  and  $a_2$  are the incident waves,  $b_1$  and  $b_2$  are the reflected waves of ports 1 and 2, and  $S_{11}$ ,  $S_{12}$ ,  $S_{21}$ , and  $S_{22}$  are the parameters of the scattering matrix  $\bar{S}$ . For our problem, we will be interested only in a reciprocal and lossless two port connected to transmission lines of equal characteristic impedance at both terminals. Reciprocity and symmetry require  $S_{12} = S_{21}$  and  $S_{11} = S_{22}$ , respectively; losslessness gives the conservation of energy relationship

$$|S_{11}|^2 + |S_{12}|^2 = 1 \quad (2)$$

$|S_{11}|^2$  is the power reflection coefficient and  $|S_{12}|^2$  is the power transmission coefficient. Hence, the magnitude of  $S_{12}$  is uniquely related to the magnitude of  $S_{11}$ . Furthermore, it can be shown<sup>7</sup> the condition

$$S_{11}S_{12}^* + S_{12}S_{22}^* = 0 \quad (3)$$

always holds for lossless, reciprocal two ports.

Equation (3) relates the phase of  $S_{22}$  to the phase of  $S_{11}$ . In fact, let

$$S_{11} = |S_{11}| e^{j\theta_1}, \quad S_{12} = |S_{12}| e^{j\theta_2},$$

then

$$\theta_2 = \theta_1 + \frac{\pi}{2} \mp n\pi. \quad (4)$$

To summarize, for the problem we are investigating, the scattering matrix description of a two-port junction consists of only two independent parameters: namely, the magnitude and phase of the reflection coefficient  $S_{11}$ .

The basic ideas of scattering are illustrated by considering two simple examples. In Fig. 3(b), a series reactance ( $jX$ ) (normalized to the line impedance) is connected in a transmission line. The incident wave is labeled  $a_1$  and the reflected wave as  $b_1 = S^-$  (assume  $a_2 = 0$ ). We can think of the transmitted wave ( $b_2$ ) as made up of two parts:  $a_1$  which exists in the absence of scattering by the series element and the scattered wave which arises because of scattering. The scattered waves ( $S^-$ ) and ( $S^+$ ) can be thought as generated by an equivalent voltage source ( $V$ ) induced by the incident wave. To see how the equivalent voltage source is related to the scattered wave, we write the following equations:

$$a_1 + b_1 - b_2 = (a_1 - b_1) jX \quad (5a)$$

or

$$S^- - S^+ = V = (a_1 - b_1) jX \quad (5b)$$

and

$$a_1 - b_1 = b_2 \quad (6a)$$

or

$$-S^- = S^+ \quad (6b)$$

Equation (5b) indicates that the voltage source is the difference of the scattered wave on either side of the series element. Furthermore, according to Eq. (6b), the scattered wave on one side is the negative of the other side. Combining Eqs. (6a) and (5a) results in the familiar expression for the reflection coefficient:

$$S_{11} = \frac{b_1}{a_1} = \frac{jX}{2 + jX} \quad (7)$$

The transmission coefficient is

$$S_{12} = \frac{b_2}{a_1} = 1 + \frac{S^+}{a_1} = \frac{2}{2 + jX} \quad (8)$$

The 1 in the expression for  $S_{12}$  is due to the complete transmission of the incident wave  $a_1$  in the absence of scattering by the series element. Obviously, conservation of energy [Eq. (2)] is satisfied.

A similar analysis for the shunt element with normalized susceptance  $jB$  in a transmission line of Fig. 3(c) gives

$$S^- + S^+ = -I \quad (9)$$

where  $I$  is the equivalent current source. Note in the shunt connection the current source is the sum of the scattered wave with

$$S^+ = S^- \quad (10)$$

The reflection coefficient is

$$S_{11} = \frac{b_1}{a_1} = \frac{-jB}{2 + jB} \quad (11)$$

transmission coefficient is

$$S_{12} = \frac{b_2}{a_1} = 1 + \frac{S_+}{a_1} = \frac{2}{2 + jB} \quad (12)$$

and conservation of energy is satisfied. We will encounter an analogous problem in the scattering of a Rayleigh wave by the rail structure.

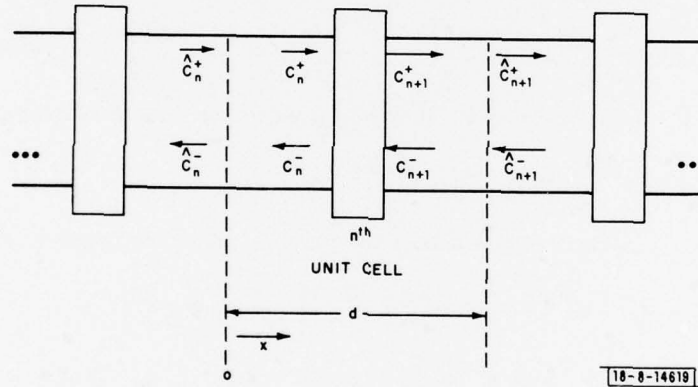


Fig. 4. Periodic transmission line.

#### B. Periodic Structure

Having reviewed the scattering matrix representation of two ports, we next take up transmission line periodically loaded with such two ports as shown in Fig. 4.

The wave amplitudes ( $\hat{C}$ 's) are related by

$$\begin{bmatrix} \hat{C}_n^+ \\ \hat{C}_n^- \end{bmatrix} = \begin{bmatrix} A_{11} e^{j\beta d} & A_{12} \\ A_{21} & A_{22} e^{-j\beta d} \end{bmatrix} \begin{bmatrix} \hat{C}_{n+1}^+ \\ \hat{C}_{n+1}^- \end{bmatrix} \quad (13)$$



where  $\beta$  is the propagation constant and the  $\bar{A}$  matrix is defined by the equation which relates the wave amplitudes (C's):

$$\begin{bmatrix} C_n^+ \\ C_n^- \end{bmatrix} = \begin{bmatrix} A_{11} & A_{12} \\ A_{21} & A_{22} \end{bmatrix} \begin{bmatrix} C_{n+1}^+ \\ C_{n+1}^- \end{bmatrix} \quad (14)$$

and  $\bar{A}$  is related to the scattering matrix  $\bar{S}$  by

$$\begin{aligned} A_{11} &= \frac{1}{S_{12}} \\ A_{21} &= -A_{12} = \frac{S_{11}}{S_{12}} \\ A_{22} &= \frac{S_{12}^2 - S_{11}^2}{S_{12}} \end{aligned} \quad (15)$$

According to Floquet's theorem, the wave amplitude at the  $(n+1)$  ST terminal can differ from the wave amplitude at  $n^{\text{th}}$  terminal by at most a phase delay. Thus, we assume

$$\begin{aligned} \hat{C}_{n+1}^+ &= e^{-j\kappa d} \hat{C}_n^+ \\ \hat{C}_{n+1}^- &= e^{-j\kappa d} \hat{C}_n^- \end{aligned} \quad (16)$$

where  $\kappa d$  is the phase delay. Substitute Eq. (16) into (13) gives an eigenvalue equation for  $\kappa$ .

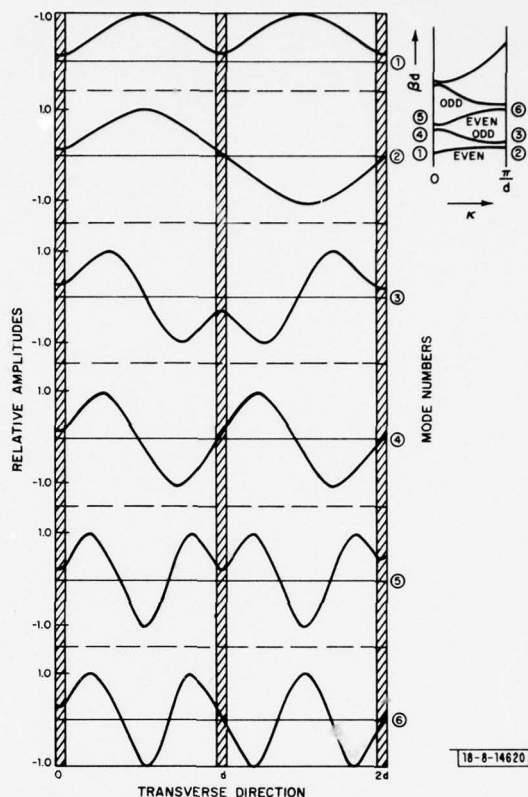
$$\cos \kappa d = \frac{1}{2S_{12}} [e^{j\beta d} + (S_{12}^2 - S_{11}^2) e^{-j\beta d}] \quad (17)$$

The characteristic modes in a particular unit cell of the periodic structure is given by

$$\begin{aligned} \varphi_n(x) &= \frac{1}{2} \left[ e^{-j\beta_n x} + \left( \frac{1}{S_{22}} e^{j\beta_n d} - \frac{S_{12}}{S_{22}} e^{j\kappa d} \right) e^{j\beta_n x} \right] \quad \text{for } 0 < x < \frac{d}{2} \\ &= \frac{1}{2} \left[ e^{-j\beta_n (x-d)} + \left( \frac{1}{S_{22}} e^{j\beta_n d} - \frac{S_{12}}{S_{22}} e^{j\kappa d} \right) e^{j\beta_n (x-d)} \right] e^{-j\kappa d} \\ &\quad \text{for } \frac{d}{2} < x < d \end{aligned} \quad (18)$$

Solution of Eq. (17) for a typical periodic structure gives the familiar dispersion diagram as shown in Fig. 5. It shows "bands" of alternating even and odd symmetry as exhibited by the mode pattern at the Brillouin zone center ( $\kappa = 0$ ) and edge ( $\kappa = \pi/d$ ). These two points are of particular interest to us because we accept as modes only those solutions which have vanishing group velocity. With a uniform excitation of the periodic rail structure, we expect from symmetry that the acoustic wave is the superposition of standing waves in the transverse direction. Furthermore, because of the assumed uniform transducer input, only symmetric modes such as modes 1 and 5 could be excited. We will refer to these modes as the fundamental mode and the higher-order mode. These two modes are most strongly excited and the beating between them gives rise to the observed spatial and frequency ripples.

Fig. 5. Dispersion diagram and modes of periodic structure.



### III. QUALITATIVE DESCRIPTION OF THE MODES

Before going into the detailed modeling of the rail structure, we now discuss qualitatively the behavior of the fundamental and higher-order modes as a function of reflection coefficient.

The fundamental and higher-order mode patterns are shown in Figs. 6(a-d) as the magnitude and phase of the reflection coefficient are varied. The magnitude of  $S_{11}$  is reduced by 50 percent in Fig. 6(b) as compared with that of Fig. 6(a). As expected, weaker reflection enables the wave function  $\varphi(x)$  to spread out from the space between the reflecting elements. The same effect can be achieved by retarding the phase of the reflection coefficient as evident in Fig. 6(c) in which phase is decreased by 40 percent from that of Fig. 6(a). A dramatic spreading effect results as shown in Fig. 6(d) if both magnitude and phase are decreased.

The spreading effect makes the fundamental mode more uniform and therefore matches better the uniform input transducer profile. Since the higher-order mode is orthogonal to the fundamental, it becomes less excited. Therefore, we can infer immediately a very important fact: in a rail structure which has a reflection coefficient with small magnitude and retardation in phase at the mode angles corresponding to the fundamental and higher-order mode, the spatial and frequency ripple size would be small.

Over the range of 50-percent variation in magnitude and 40-percent variation in phase, the mode patterns basically retain their shapes (i.e., nearly one half-cycle of sinusoid for the fundamental and three half-cycles for the higher-order mode). This indicates that the mode

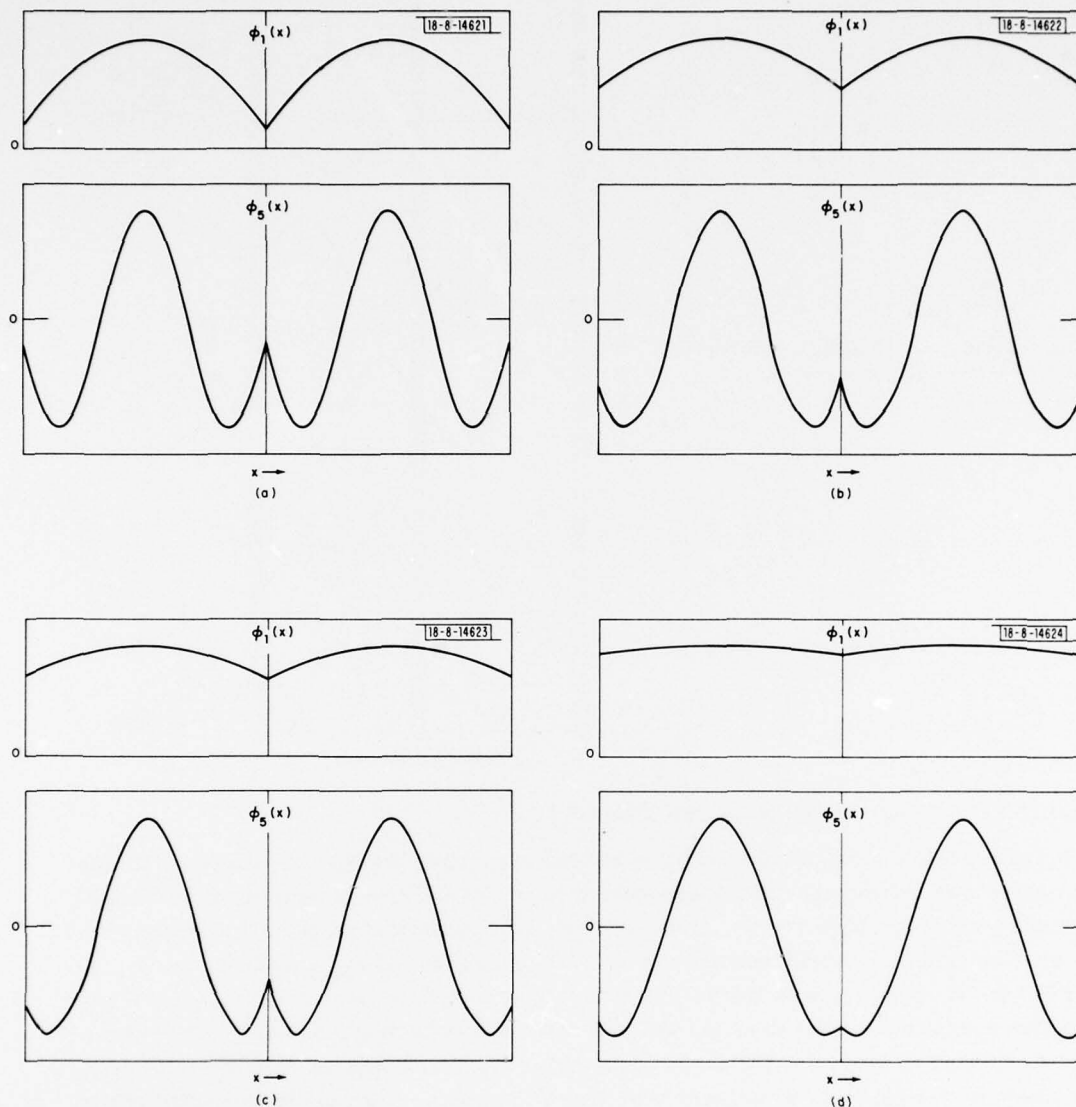


Fig. 6. Mode profiles of periodic rail structure: (a)  $S_{11} = 0.955 \exp j(3.037)$ , (b)  $S_{11} = 0.478 \exp j(3.037)$ , (c)  $S_{11} = 0.955 \exp j(1.822)$ , and (d)  $S_{11} = 0.478 \exp j(1.822)$ .



pattern is not strongly dependent on the reflection coefficient. Its shape is inherently a characteristic of the periodicity.

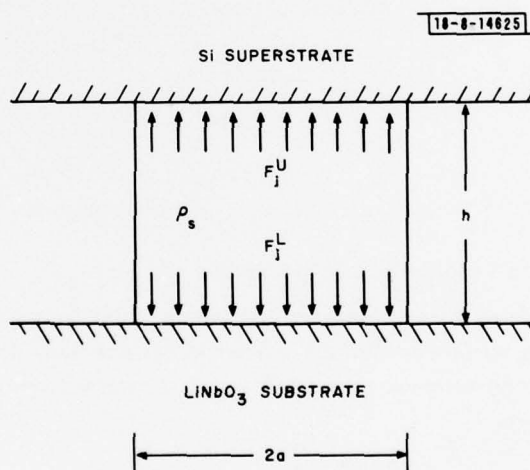
For the range of variation in reflection coefficient studied, the beat length varies from 80 to  $154 \lambda_R$  assuming a periodicity of  $9 \lambda_R$ . As the modes spread out more uniformly, the transverse wave vector becomes smaller, forcing the longitudinal wave vectors of the modes to approach more closely with each other, therefore, the beat length tends to increase.

Now suppose the spacing is reduced, but assume the reflection coefficients remain unchanged for the fundamental and higher-order mode. Then the transverse wave vectors increase linearly, resulting in shorter longitudinal wave vectors; but the length difference is greater, hence, a smaller beat length. In reality, reducing the spacing means increasing the mode angle and, thus, the reflection coefficients do not remain constant but in fact would decrease causing the modes to spread more uniformly. It is not clear, without a more detailed model of the ridge structure, which is the dominant effect on the beat length. As shown in Sec. V, the dependence of reflection coefficient on mode angle is not strong enough to overcome the dominant longitudinal wave vector length-difference effect. The net result of decreasing the spacing is to decrease the beat length. At the same time, since the modes are more uniformly spread out, the ripple size would decrease.

#### IV. SCATTERING MATRIX REPRESENTATION OF THE RAIL STRUCTURE

With the framework of periodically loaded transmission set, we are now ready to study in more detail the physics of the rail structure. In particular, we are interested in characterizing the scattering of a Rayleigh wave by the rail structure (Fig. 7) in terms of its scattering matrix.

Fig. 7. Scattering geometry of a point source.



The basic idea in solving the scattering problem is to find an equivalent source of scattering, in our case a stress tensor, in place of the line discontinuity. The stress tensor must satisfy boundary conditions specified by the dynamics of the rail in the presence of the incident Rayleigh wave. For example, suppose the rail is pinned so that no motion is allowed. This can be realized by assuming an infinitely massive rail or an infinitely stiff superstrate. Then, to satisfy the pinned boundary condition, there must be an equivalent stress at the position of the rail causing a displacement which exactly cancels the displacement of the incident wave and

of the scattered wave as sensed by the source. The effect of the scattered Rayleigh field must be included in the figuring of equivalent sources because the scattered field reacts back on the source which produced it in the first place. This feedback phenomenon is encountered in other scattering problems as well and is very important if conservation of energy is to be satisfied. Notice that we have allowed only the surface wave in this feedback process. The bulk wave is ignored because it is not found experimentally to be significant.<sup>6</sup>

To find the source which satisfies the near-field boundary condition, we must know for a given point stress what is the displacement in the neighborhood of the source. In other words, we like to evaluate the dynamic Green's function near the origin where the source is located. As it turned out, the dynamic Green's function within a distance from the origin, which is small compared with the wavelength, is identical to the static Green's function. An analogous situation occurs in electromagnetic problems. The near field of an oscillating dipole is equal to the quasi-static dipole field. We will justify this equivalence in more detail later when we study the Fourier integral expression of the Green's function. The asymptotic far-field evaluation of the Fourier integral at the Rayleigh pole gives the scattered surface wave.

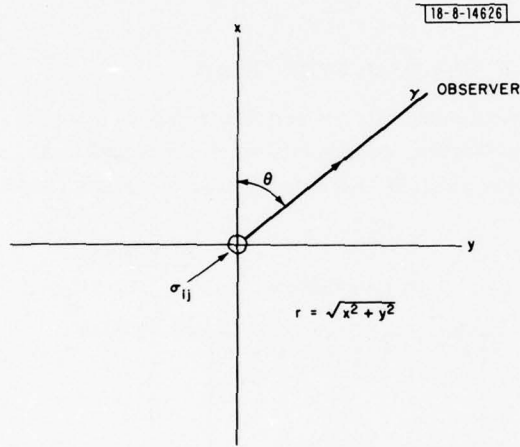


Fig. 8. Rail-support structure.

#### A. Green's Function of a Point Source

Suppose stress  $\sigma_{ij}$  with Fourier transform  $\sigma_{ij}(k)$  is applied at the origin of the x-y plane as shown in Fig. 8; we like to find the scattered surface wave on an isotropic medium with Lamé constants  $\lambda, \mu$ . Assume the potentials  $\varphi$  and  $\psi$ , respectively, for the compressional and shear waves of the form:

$$\varphi = C e^{-j(k_x x + k_y y)} e^{-pz} \quad (19)$$

$$\psi = jS e^{-j(k_x x + k_y y)} e^{-sz} \quad (20)$$

where

$$k_x^2 + k_y^2 - p^2 = k_1^2 \quad (21)$$

$$k_x^2 + k_y^2 - s^2 = k_2^2 \quad (22)$$

$$k^2 = k_x^2 + k_y^2 \quad (23)$$

$$k_1 = \omega \left( \frac{\rho}{\lambda + 2\mu} \right)^{1/2} \quad (24)$$

and

$$k_2 = \omega \left( \frac{\rho}{\mu} \right)^{1/2} \quad (25)$$

where  $\rho$  is the mass density.

Suppose a surface stress exists, Fourier decomposition gives<sup>8</sup>

$$C(k) = \frac{(k^2 + s^2) \sigma_{zz}(k) + j2ks [\sigma_{xz}(k) \cos \theta + \sigma_{yz}(k) \sin \theta]}{\mu D(k)} \quad (26)$$

$$S(k) = \frac{2kp \sigma_{zz}(k) + j(k^2 + s^2) [\sigma_{xz}(k) \cos \theta + \sigma_{yz}(k) \sin \theta]}{\mu D(k)} \quad (27)$$

where

$$D(k) = (k^2 + s^2)^2 - 4k^2 ps \quad (28)$$

and  $\theta$  is the angle the line of observation ( $y$ -axis) makes with the  $x$ -axis. The angular dependence comes from the projection of the shear stress components onto the line of observation. The reason is that only the shear stress pointing along the direction of observation couples with the Rayleigh wave in that direction. Taking superposition of all spatial harmonics, we have:

$$\varphi(x, y, z) = \int_{-\infty}^{\infty} dk_x \int_{-\infty}^{\infty} dk_y C(k) e^{-j(k_x x + k_y y)} e^{-pz} \quad (29)$$

$$\psi(x, y, z) = \int_{-\infty}^{\infty} dk_x \int_{-\infty}^{\infty} dk_y jS(k) e^{-j(k_x x + k_y y)} e^{-sz} \quad (30)$$

For a point stress with the total applied force components  $F_x$ ,  $F_y$ , and  $F_z$ ,

$$\sigma_{zz} = -F_z \delta(x) \delta(y) \quad (31)$$

$$\sigma_{xz} = -F_x \delta(x) \delta(y) \quad (32)$$

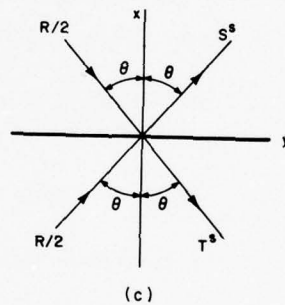
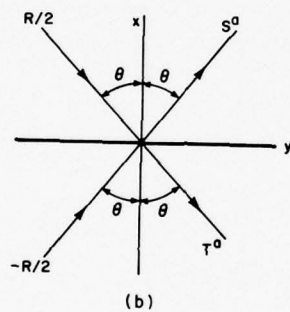
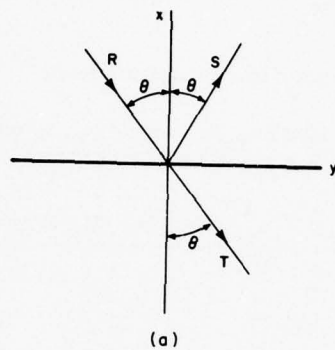
$$\sigma_{yz} = -F_y \delta(x) \delta(y) \quad (33)$$

the Green's function is

$$\begin{aligned} \varphi^G(x, y, z) = & \frac{1}{(2\pi)^2} \int_{-\infty}^{\infty} dk_x \int_{-\infty}^{\infty} dk_y \frac{-(k^2 + s^2) F_z - j2ks(F_x \cos \theta + F_y \sin \theta)}{\mu D(k)} \\ & \times e^{-j(k_x x + k_y y)} e^{-pz} \end{aligned} \quad (34)$$

$$\begin{aligned} \psi^G(x, y, z) = & \frac{j}{(2\pi)^2} \int_{-\infty}^{\infty} dk_x \int_{-\infty}^{\infty} dk_y \frac{-2kpF_z - j(k^2 + s^2)(F_x \cos \theta + F_y \sin \theta)}{\mu D(k)} \\ & \times e^{-j(k_x x + k_y y)} e^{-sz} \end{aligned} \quad (35)$$





$$S = S^a + S^s$$

$$T = T^a + T^s$$

Fig.9. Geometry of rail scattering: (a) net excitation, (b) antisymmetric, and (c) symmetric components.

Now, using Eqs. (34) and (35), we justify our earlier claim that the dynamic Green's function near the source appears quasi-static. Within distance of the order of a wavelength, integration in  $k$ -space does not show any special dependence until  $k_x$  and  $k_y$  are much greater than  $2\pi/\lambda_R$  or larger than either  $k_1$  or  $k_2$ . In this range the integrand in Eqs. (34) and (35) is independent of frequency. Therefore,  $\phi^G$  and  $\psi^G$  are identical with the static Green's function in the neighborhood of the source.

#### B. Static Green's Function of a Point Source

The static Green's function for the displacement due to a point stress is given by Landau and Lifshitz.<sup>9</sup>

$$U_x = \frac{1+\sigma}{2\pi E} \frac{1}{r} \left[ \frac{-(1-2\sigma)x}{r} F_z + 2(1-\sigma) F_x + \frac{2\sigma x}{r^2} (xF_x + yF_y) \right] \quad (36)$$

$$U_y = \frac{1+\sigma}{2\pi E} \frac{1}{r} \left[ \frac{-(1-2\sigma)y}{r} F_z + 2(1-\sigma) F_y + \frac{2\sigma y}{r^2} (xF_x + yF_y) \right] \quad (37)$$

$$U_z = \frac{1+\sigma}{2\pi E} \frac{1}{r} \left[ 2(1-\sigma) F_z + (1-2\sigma) \frac{1}{r} (xF_x + yF_y) \right] \quad (38)$$

where  $E$  is the Young's modulus,  $\sigma$  is the Poisson ratio, and  $r$  is the distance from the source. Equations (36) to (38) pertain to a point stress and therefore are not directly applicable to our rail problem which has a line geometry. However, as we will see later, these equations are directly applicable to the post problem. In the next section we will derive the counterparts of Eqs. (36) to (38) for the rail problem.

#### C. Green's Function of a Modulated Line Source

Figure 9(a) illustrates the geometry of scattering for the rail structure. The rail is assumed to lie along the  $y$ -axis with the Rayleigh wave incident at an angle  $\theta$  with respect to the  $x$ -axis and the reflected wave going off also at angle  $\theta$ .

We will assume an equivalent modulated line source along the  $y$ -axis. The modulation  $e^{-jk_y y}$  comes from the fact that the incident Rayleigh wave has  $e^{-jk_y y}$  dependence. Analogous to Eqs. (34) and (35), we take a Fourier superposition of space harmonics now only in the  $k_x$  dimension.

$$\phi^G(x, y, z) = \frac{1}{2\pi} \int_{-\infty}^{\infty} dk_x \frac{-(k^2 + s^2) F_z - j2ks(F_x \cos \theta + F_y \sin \theta)}{\mu D(k)} e^{-j(k_x x + k_y y)} e^{-pz} \quad (39)$$

$$\psi^G(x, y, z) = \frac{j}{2\pi} \int_{-\infty}^{\infty} dk_x \frac{-2kpF_z - j(k^2 + s^2)(F_x \cos \theta + F_y \sin \theta)}{\mu D(k)} e^{-j(k_x x + k_y y)} e^{-sz} \quad (40)$$

where the modulated line source is

$$\sigma_{zz} = -F_z e^{-jk_y y} \delta(x) \quad (41)$$

$$\sigma_{xz} = -F_x e^{-jk_y y} \delta(x) \quad (42)$$

$$\sigma_{yz} = -F_y e^{-jk_y y} \delta(x) \quad (43)$$

The integration in Eqs. (39) and (40) can be done easily, by picking up the Rayleigh pole residue at  $k_x = \sqrt{k_R^2 - k_y^2}$  where  $k_R = 2\pi/\lambda_R$  is the propagation constant of the Rayleigh wave; the integrations are done in Appendix A. The results are repeated here for convenience.

$$\varphi^G(r, z) = \frac{-2k_R s (F_y \sin \theta \pm F_x \cos \theta) + j(2k_R^2 - k_2^2) F_z}{\mu D'(k_R) \cos \theta} e^{-jk_R r} e^{-pz} \quad (44)$$

$$\psi^G(r, z) = \frac{-j(2k_R^2 - k_2^2) (F_y \sin \theta \pm F_x \cos \theta) - (2k_R p) F_z}{\mu D'(k_R) \cos \theta} e^{-jk_R r} e^{-sz} \quad (45)$$

The Green's functions for displacement  $U_r$  and  $U_z$  of the Rayleigh wave on the surface ( $z = 0$ ) are then

$$\begin{aligned} U_r &= \frac{\partial \varphi}{\partial r} - \frac{\partial \psi}{\partial z} \\ &= \frac{e^{-jk_R r}}{\mu D'(k_R) \cos \theta} [k_R (2k_R^2 - k_2^2 - 2ps) F_z + jk_2^2 s (F_y \sin \theta \pm F_x \cos \theta)] \end{aligned} \quad (46)$$

$$\begin{aligned} U_z &= \frac{\partial \varphi}{\partial z} + \frac{\partial \psi}{\partial r} \\ &= \frac{e^{-jk_R r}}{\mu D'(k_R) \cos \theta} [jk_2^2 p F_z - k_R (2k_R^2 - k_2^2 - 2ps) (F_y \sin \theta \pm F_x \cos \theta)] \end{aligned} \quad (47)$$

To simplify notation, Eqs. (46) and (47) are written in tensor form:

$$U_i = E_{ij} F_j e^{-jk_R r} \quad (48)$$

where

$$E_{11} = \frac{\pm jk_2^2 s \cos \theta}{\mu D'(k_R)} \quad (49)$$

$$E_{12} = \frac{jk_2^2 s \sin \theta}{\mu D'(k_R)} \quad (50)$$

$$E_{13} = \frac{k_R (2k_R^2 - k_2^2 - 2ps)}{\mu D'(k_R)} \quad (51)$$

$$E_{21} = \frac{\pm jk_2^2 s \sin \theta}{\mu D'(k_R)} \quad (52)$$

$$E_{22} = \frac{+jk_2^2 s \sin^2 \theta}{\mu D'(k_R) \cos \theta} \quad (53)$$

$$E_{23} = -E_{32} = \frac{k_R (2k_R^2 - k_2^2 - 2ps) \sin \theta}{\mu D'(k_R) \cos \theta} \quad (54)$$

$$E_{31} = \frac{\mp k_R (2k_R^2 - k_2^2 - 2ps)}{\mu D'(k_R)} \quad (55)$$

$$E_{33} = \frac{jk_2^2 p}{\mu D'(k_R) \cos \theta} \quad (56)$$

#### D. Stiffness Matrix

The near field of a modulated line source approaches that of the quasi-static Green's function. We assume the force is uniformly distributed across the width of the rail (a good assumption if the width  $\ll \lambda_R$ ) and sinusoidally modulated with a phase factor  $e^{-jk_y y}$  along the length of the rail. The displacements at the center  $x = 0$  are found by convolutions of Eqs. (36) to (38). This is done in Appendix B. The result is given in the form

$$U_i = T_{ij} F_j \quad (57)$$

where  $T_{ij}$  is a diagonal tensor which measures the stiffness of the medium.

#### E. Reaction of Scattered Wave on the Source

As in any acoustic scattering process, the scattered wave tends to react back on the source of scattering. The interaction of the scattered wave with the source was illustrated in Sec. II using the examples of series and shunt elements in a transmission line. Now we want to see explicitly how this interaction occurs in the case of scattering of a Rayleigh wave by the rail structure.

A great deal can be deduced from the symmetry of the problem. For example,  $F_x$  excites only a surface wave of odd symmetry with respect to the  $y$ -axis, while  $F_z$  and  $F_y$  excite surface waves of even symmetry. Therefore,  $F_x$  does not "feel" the scattered wave generated by  $F_z$  or  $F_y$  and vice versa. Stated in another way,  $F_x$  does not couple with  $F_z$  or  $F_y$ ; however,  $F_z$  and  $F_y$  do couple with each other. This observation suggests the scattering of a Rayleigh wave can be viewed as being made up of an antisymmetric scattering in the  $x$ -direction and a symmetric scattering in the  $y$ - and  $z$ -direction. Indeed, as we shall see later, this turns out to be the case.

Let  $\langle U_i \rangle$  denote the average of the scattered wave which reacts back on the source. Then we can relate  $\langle U_i \rangle$  to  $F_j$  by the following matrix equation.

$$\begin{bmatrix} \langle U_x \rangle \\ \langle U_y \rangle \\ \langle U_z \rangle \end{bmatrix} = \begin{bmatrix} V_{11} & 0 & 0 \\ 0 & V_{22} & V_{23} \\ 0 & V_{32} & V_{33} \end{bmatrix} \begin{bmatrix} F_x \\ F_y \\ F_z \end{bmatrix} \quad (58)$$

where

$$\begin{aligned} V_{11} &= E_{11}(+) \quad , \\ V_{22} &= E_{22} \quad , \\ V_{23} &= -V_{32} = E_{23} \quad , \\ V_{33} &= E_{33} \quad . \end{aligned}$$



The "averaging" is taken so that  $F_x$  "feels" the difference of the scattered wave [analogous to Eq. (5b) for scattering by a series element in a transmission line], while  $F_y$  and  $F_z$  "feel" the sum of the scattered wave [analogous to Eq. (9) for scattering by a shunt element in a transmission line].

#### F. Dynamic Equation of the Rail Structure

The boundary condition satisfied by the sources  $F_j$  obey the dynamic equations:

$$U_i^R + T_{ij}^L F_j^L + \langle U_i \rangle = T_{ij}^U F_j^U \quad (59)$$

and

$$-(F_j^L + F_j^U) = -2ah\rho_s \omega^2 U_j \quad (60)$$

Referring to Fig. 7,  $T_{ij}^U$  and  $T_{ij}^L$  are the stiffness tensors of the upper and lower substrate with applied force per unit length  $F_j^U$  and  $F_j^L$ , respectively,  $2a$  is the width,  $h$  is the height,  $\rho_s$  is the mass density of the spacer,  $U_i^R$  is the incident Rayleigh displacement, and  $U_j$  is the net displacement. The displacements  $U_i^R$  at the surface  $z = 0$  are given by<sup>8</sup>

$$U_x^R = jA_+ \frac{k_2^2}{2k_R} e^{-j(k_x x + k_y y)} \cos \Theta \quad (61)$$

$$U_y^R = -jA_+ \frac{k_2^2}{2k_R} e^{-j(k_x x + k_y y)} \sin \Theta \quad (62)$$

$$U_z^R = A_+ \frac{2k_R^2 - k_2^2 - 2sp}{2s} e^{-j(k_x x + k_y y)} \quad (63)$$

Substitution of Eqs. (60) and (58) into Eq. (59) yields

$$[T_{ij}^U + T_{ij}^L - 2ah\rho_s \omega^2 T_{il}^U (T_{lj}^L + V_{lj}) + V_{ij}] F_j = -(\delta_{ij} - 2ah\rho_s \omega^2 T_{ij}^U) U_j^R \quad (64)$$

where  $\delta_{ij}$  is the Kronecker delta. Let

$$G_{ij} = T_{ij}^U + T_{ij}^L - 2ah\rho_s \omega^2 T_{il}^U (T_{lj}^L + V_{lj}) + V_{ij} \quad (65)$$

and

$$R_{ij} = -(\delta_{ij} - 2ah\rho_s \omega^2 T_{ij}^U) \quad (66)$$

Equation (64) becomes

$$\begin{bmatrix} G_{11} & 0 & 0 \\ 0 & G_{22} & G_{23} \\ 0 & G_{32} & G_{33} \end{bmatrix} \begin{bmatrix} F_x \\ F_y \\ F_z \end{bmatrix} = \begin{bmatrix} R_{11} & U_x^R \\ R_{22} & U_y^R \\ R_{33} & U_z^R \end{bmatrix} \quad (67)$$

The form of the matrix equation (67) confirms the fact that antisymmetric scattering in the x-direction is independent of the symmetric scattering in the z- or y-directions.

#### G. Scattering Matrix of the Rail Structure

To find the scattering matrix of the rail structure, we consider an incident Rayleigh wave R with displacements  $U_j^R$  launched at angle  $\theta$  with respect to the x-axis against the rail [see Fig. 9(a)]. The reflected wave S and transmitted wave T have displacements  $U_j^S$  and  $U_j^T$ , respectively. Because the displacements of the Rayleigh wave are related to each by definite ratios [see Eqs. (61) to (63)], we can define a set of unique scattering matrix coefficients from the ratios of the z-displacements of S and T waves to the z-displacement of the R wave, i.e.,

$$S_{11} = \frac{U_Z^S}{U_Z^R} \quad (68)$$

and

$$S_{12} = \frac{U_Z^T}{U_Z^R} \quad (69)$$

$U_Z^R$ ,  $U_Z^S$ , and  $U_Z^T$  have one-to-one correspondence with voltages  $a_1$ ,  $b_1$ , and  $b_2$ , respectively, of the transmission line model shown in Fig. 3(a). The excitation of Fig. 9(a) can be decomposed into its antisymmetric part [Fig. 9(b)] and symmetric part [Fig. 9(c)]. Indeed, by adding the displacement components of the antisymmetric excitation to that of the symmetric excitation, we get exactly the displacements of the original excitation represented in Fig. 9(a).

In the antisymmetric excitation, all the incident Rayleigh displacement components cancel except the x-component which is equal to the x-displacement component of the R wave. Solving for  $F_x$  in Eq. (67), substituting into Eq. (48), we find the antisymmetric scattered field normalized to the incident field to be

$$\begin{aligned} D^a &= E_{31}^{(-)} \frac{F_x}{U_Z^R} \\ &= \frac{jX^a}{1 + jX^a} \end{aligned} \quad (70)$$

where

$$X^a = \frac{k_2^2 s}{\mu D^{(k_R)}} \frac{(1 - 2ah\rho_s \omega^2 T_{11}^U) \cos \theta}{T_{11}^L (1 + T_{11}^U / T_{11}^L - 2ah\rho_s \omega^2 T_{11}^U)} \quad (71)$$

Therefore, we find for the antisymmetric excitation:

$$\Gamma^a = \frac{U_Z^{(S^a)}}{U_Z^R} = -\frac{1}{2} + D^a = \frac{1}{2} \frac{-1 + jX^a}{1 + jX^a} \quad (72)$$

and

$$\tau^a = \frac{U_Z^{(T^a)}}{U_Z^R} = \frac{1}{2} - D^a = \frac{1}{2} \frac{1 - jX^a}{1 + jX^a} \quad (73)$$

The  $-1/2$  in Eq. (72) is due to the total transmission of the incident wave  $-R/2$  from the bottom side in the absence of scattering; similar reason explains the  $1/2$  in Eq. (73).

For symmetric excitation, the x-component of the incident Rayleigh wave displacement cancels leaving the y-component and z-component which are equal to the y- and z-displacement components of the R wave. The symmetric scattered field is found by first solving for  $F_y$  and  $F_z$  in Eq. (67) and then substituting into Eq. (48), we find

$$\begin{aligned} D^S &= \frac{E_{32}F_y + E_{33}F_z}{U_z^R} \\ &= \frac{-jB^S}{2 + jB^S} \end{aligned} \quad (74)$$

where

$$\begin{aligned} B^S &= \frac{2k_z^2}{\mu D'(k_R) \cos \theta} \left[ p \left( \frac{1 - 2ah\rho_s \omega^2 T_{33}^U}{T_{33}^L} \right) (1 + T_{22}^U/T_{22}^L - 2ah\rho_s \omega^2 T_{33}^U) \right. \\ &\quad \left. + s \sin^2 \theta \left( \frac{1 - 2ah\rho_s \omega^2 T_{22}^U}{T_{22}^L} \right) (1 + T_{33}^U/T_{33}^L - 2ah\rho_s \omega^2 T_{33}^U) \right] / \\ &\quad (1 + T_{22}^U/T_{22}^L - 2ah\rho_s \omega^2 T_{22}^U) (1 + T_{33}^U/T_{33}^L - 2ah\rho_s \omega^2 T_{22}^U) \end{aligned} \quad (75)$$

Thus, for the symmetric excitation:

$$\Gamma^S = \frac{U_z^{(S)}}{U_z^R} \approx \frac{1}{2} + D^S = \frac{1}{2} \frac{2 - jB^S}{2 + jB^S} \quad (76)$$

$$\tau^S = \frac{U_z^{(T)}}{U_s^R} = \frac{1}{2} + D^S \approx \frac{1}{2} \frac{2 - jB^S}{2 + jB^S} \quad (77)$$

Finally, the scattering matrix coefficients of the original excitation [Fig. 9(a)] are found by superposition:

$$\begin{aligned} S_{11} &= \frac{U_z^S}{U_z^R} \\ &= \frac{U_z^{(S^a)} + U_z^{(S^S)}}{U_z^R} \\ &= D^a + D^S \\ &= \frac{jX^a}{1 + jX^a} - \frac{jB^S}{2 + jB^S} \end{aligned} \quad (78)$$

and

$$\begin{aligned}
 S_{12} &= \frac{U_z^T}{U_z^R} \\
 &= \frac{U_z^{(T^a)} + U_z^{(T^s)}}{U_z^R} \\
 &= 1 - D^a + D^s \\
 &= 1 - \frac{jX^a}{1 + jX^a} - \frac{jB^s}{2 + jB^s} \quad . \quad (79)
 \end{aligned}$$

#### H. Conservation of Energy

An important test of the validity of  $S_{11}$  and  $S_{12}$  given by Eqs. (78) and (79) is to show that the conservation of energy is satisfied.

$$\begin{aligned}
 |S_{11}|^2 + |S_{12}|^2 &= \left| \frac{jX^a}{1 + jX^a} - \frac{jB^s}{2 + jB^s} \right|^2 + \left| 1 - \frac{jX^a}{1 + jX^a} - \frac{jB^s}{2 + jB^s} \right|^2 \\
 &= 1 \quad \text{Q.E.D.} \quad (80)
 \end{aligned}$$

This condition becomes obvious by noting  $\Gamma$ 's and  $\tau$ 's of Eqs. (72), (73), (76), and (77) have magnitude of 1/2 implying conservation of energy holds for the antisymmetric part and symmetric part of scattering as it must.

### V. RESULTS ON THE RAIL STRUCTURE

In this section, we present calculations of the reflection coefficient and modes of the periodic rail structure using the model described in the previous section.

#### A. Reflection Coefficient

Figure 10 plots the fraction of reflected power,  $|S_{11}|^2$ , of the ridge vs the angle of incidence  $\theta$ . As expected,  $|S_{11}|^2$  increases with angle of incidence and approaches unity at grazing

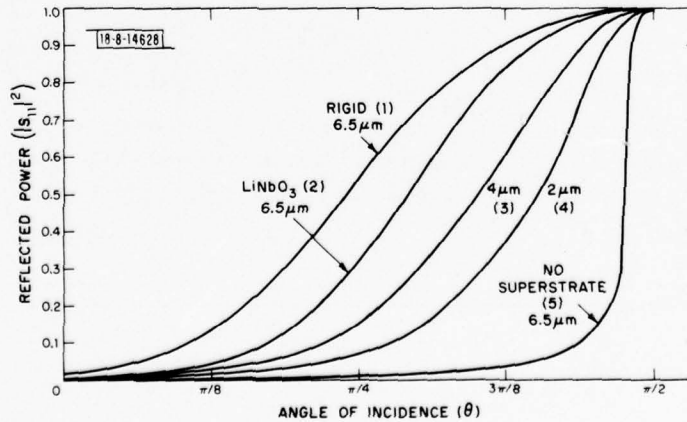


Fig. 10. Reflection of Rayleigh wave by the rail structure.



TABLE I WAVEGUIDE PARAMETERS							
Rail Support		Fundamental Mode		Higher-Order Mode		Interaction	
Width ( $\mu\text{m}$ )	Spacing ( $\mu\text{m}$ )	$\beta_1 d$	$ s_{11} ^2$	$\beta_3 d$	$ s_{11} ^2$	$L_b (\lambda_R)$	M (dB)
6.5	100	3.06	0.998	9.18	0.976	86	-1.91
4	100	2.96	0.991	8.89	0.920	92	-1.82
2	100	2.84	0.977	8.56	0.815	99	-1.64
2	30	2.35	0.842	7.47	0.278	11	-0.73
4	363	3.09	0.999	9.27	0.993	1119	-1.93
$f = 300 \text{ MHz}$ $V_R = 3308 \text{ m/sec}^\dagger$ $\lambda_R = 11 \mu\text{m}^\dagger$ $\rho_s = 4700 \text{ kg/m}^3 \text{ (LiNbO}_3\text{)}, 2330 \text{ kg/m}^3 \text{ (Si)}$ $\left\{ \begin{array}{l} \lambda = 8.3 \times 10^{10} \text{ N/m}^3 \text{ (LiNbO}_3\text{)}, 6.39 \times 10^{10} \text{ N/m}^3 \text{ (Si)} \\ \mu = 6.0 \times 10^{10} \text{ N/m}^3 \text{ (LiNbO}_3\text{)}, 7.96 \times 10^{10} \text{ N/m}^3 \text{ (Si)} \end{array} \right.$ $h = 3000 \text{ \AA}$							
$\dagger$ These values are calculated from the assumed Lamé constants.							

incidence ( $\theta = \pi/2$ ). The reason is because the ridge appears to be "softer" for a Rayleigh wave incident at a small angle as evident by looking at the stiffness matrix  $\tau_{ij}$  of Eqs. (B-10) to (B-12).

The mass of the spacer makes little difference in the reflection coefficient as shown by the curve labeled (2) corresponding to the case of  $\text{LiNbO}_3$ , Si, and zero mass. On the other hand, the scattering of the Rayleigh wave is very sensitive to the stiffness of the superstrate. For example, by letting the superstrate become infinitely stiff (curve 1) the reflection increases. On the other hand, removal of the superstrate (curve 5) leads to a dramatic decrease in the reflectivity. The effect of the superstrate is to deaden the surface vibration. This effect is enhanced by a wider ridge as evident in curves 2, 3, and 4 where the width is changed from 6 to 4  $\mu\text{m}$  and then to 2  $\mu\text{m}$ . Although not shown in Fig. 10, the phase of the reflection coefficient generally decreases with a decrease in the magnitude except for the case of no superstrate.

#### B. Modes of the Periodic Rail Structure

Using the scattering matrix coefficients of the ridge, we proceed to find the modes of the periodic rail structure using Eq. (17). The results are summarized in Table I. We have studied the behavior of the fundamental mode and the higher-order mode by changing the width and the spacing of the rail. The resulting mode profiles are given in Figs. 11 to 14. Beat length and frequency ripple are also calculated.

The mode expansion of the uniform input is given by

$$\sum_{i=1}^{\infty} a_i N_i \varphi_i(x) = 1 \quad (81)$$

where  $\varphi_i(x)$  is the mode profile given by Eq. (18) with unity peak amplitude,  $N_i$  is the normalization constant such that

$$\int_0^d N_i^2 \varphi_i^2(x) dx = 1 \quad (82)$$

$$N_i = \left[ \frac{1}{2\beta_i} (\beta_i d + \sin \beta_i d) \right]^{-1/2} \quad (83)$$

where  $\beta_i d$  is the normalized transverse wave number, and

$$a_i = \int_0^d N_i \varphi_i(x) dx = \frac{2N_i}{\beta_i} \sin \frac{\beta_i d}{2} \quad (84)$$

The modes of a 6.5- $\mu\text{m}$ -wide periodic rail structure with 100- $\mu\text{m}$  spacing are shown in Fig. 11. Superposition of the fundamental and higher-order mode according to Eq. (81) gives the field profiles of Fig. 12 depending on the relative phase of the modes, given by the longitudinal propagation phase factor  $e^{-j\epsilon_i y}$  where

$$\epsilon_i = \sqrt{k_R^2 - \beta_i^2} \quad (85)$$

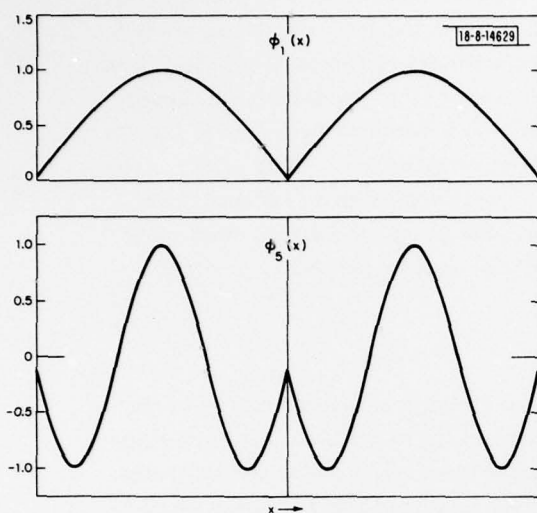


Fig. 11. Mode profiles of 6.5- $\mu\text{m}$  rail structure with 100- $\mu\text{m}$  spacing.

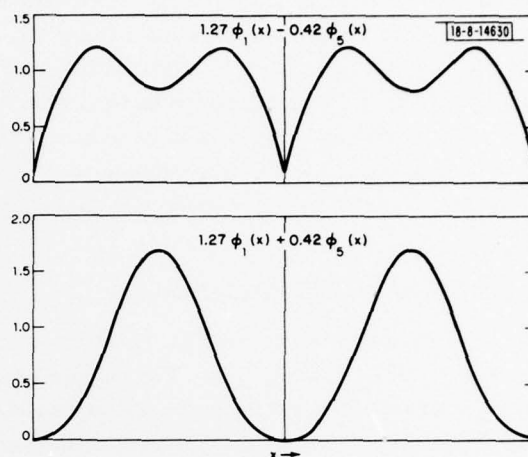


Fig. 12. Superposition of mode profiles.

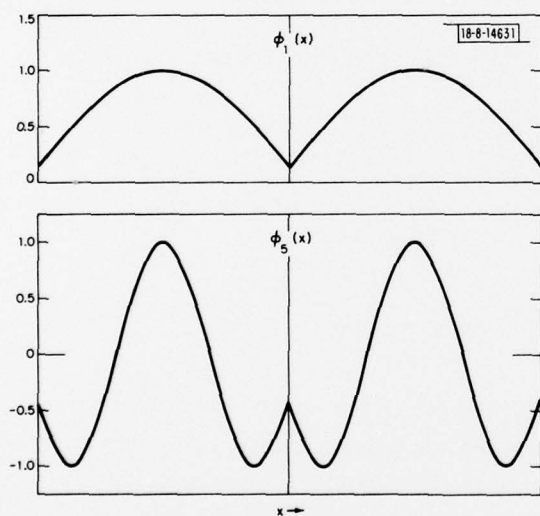


Fig. 13. Mode profiles of 2- $\mu\text{m}$  rail structure with 100- $\mu\text{m}$  spacing.

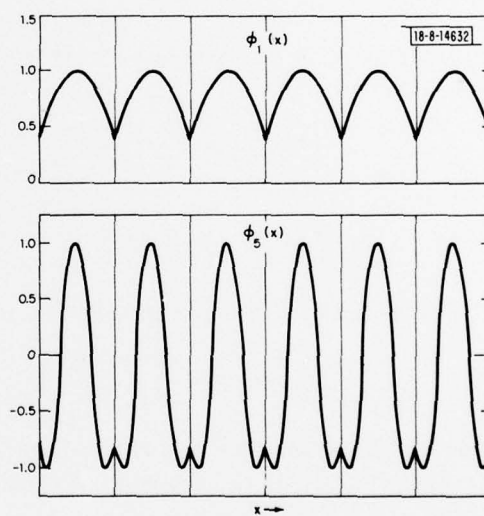


Fig. 14. Mode profiles of 2- $\mu\text{m}$  rail structure with 30- $\mu\text{m}$  spacing.

we can get either the sum or the difference of the two modes resulting in a beat pattern. Spatially, at a fixed frequency, the superposed field profile repeats within a distance  $L_b$ , the beat length, such that

$$L_b(\xi_1 - \xi_5) = 2\pi \quad . \quad (86)$$

The beat pattern also occurs at the output transducer as the frequency is swept. The frequency interval  $\Delta f$  is related to  $L_b$  by

$$\frac{\Delta f}{f} = \frac{L_b}{L} \quad (87)$$

where  $L$  is the distance between the input and output transducer. The depth of ripple as detected in the received power as a function of frequency is

$$M = 20 \log \left( \frac{a_1^2 - a_5^2}{a_1^2 + a_5^2} \right) \quad . \quad (88)$$

Table I shows that for the 6.5- $\mu\text{m}$  device, the beat length is  $86 \lambda_R$  as compared with  $137 \lambda_R$  measured experimentally<sup>6</sup> (Fig. 1). The ripple frequency depth is -1.9 dB, somewhat less than the -3 dB observed in the output frequency response (Fig. 2). The discrepancy is probably caused by groove scattering not included in our present model.

Figure 13 shows the modes in the rail structure with narrower width but with the same spacing. Because the reflectivity is reduced and phase retarded, the modes become more spread out resulting in longer beat length and smaller ripple (see Table I) as explained in Sec. III. To take advantage of the mode-spreading effect with weaker reflectivity, the width is made narrower and the spacing is reduced. The latter allows the mode angles to be smaller (i.e., closer to normal incidence), therefore achieving a weaker reflection coefficient. The spacing is decreased for another important reason. By increasing the number of supports, the load supported by each rail is decreased; as a result, the deformation is kept small, minimizing groove scattering. The combined effect is seen by the mode profiles shown in Fig. 14 for a structure with 2- $\mu\text{m}$  width and 30- $\mu\text{m}$  spacing. It is clear that the modes have indeed spread out significantly as compared with those of Fig. 11. Consequently, as shown in Table I, the depth of ripple has reduced to -0.73 dB. However,  $L_b$  has shortened to  $11 \lambda_R$ .

A word of caution, by continuing the reduction of the rail width, eventually groove scattering caused by larger deformation near the rail becomes important. The effect of groove scattering is certainly to increase the magnitude of reflection coefficient. However, it is not clear without further study which way the phase will change. If the phase is retarded, then the modes tend to be spread out offsetting the effect of the increased reflectivity. In addition, bulk scattering may now play an important role as the groove is steepened and more rails are in place as a result of reducing the spacing. A definitive judgment cannot be made until we study more closely the coherent bulk scattering by an array of rails.

## VI. POST SCATTERING

In this section, we take up the post scattering problem. It is solved in a similar fashion as the rail scattering problem. We first of all evaluate asymptotically the far field from the



integral expression of the Green's function of a point source derived in Sec. IV. Then, the stiffness matrix and the dynamic equation are derived. Finally, we present the radiation patterns of post scattering.

#### A. Green's Function

Integral expressions of the Green's function are given in Eqs. (34) and (35). In Appendix C, the scattered Rayleigh wave is evaluated. The results are

$$\begin{aligned} \varphi^G(r, z) = & \left(\frac{j}{2\pi}\right)^{1/2} \frac{1}{\sqrt{k_R r}} \frac{-2k_R s(F_y \sin \Theta + F_x \cos \Theta) + j(2k_R^2 - k_2^2) F_z}{\mu D'(k_R)/k_R} \\ & \times e^{-jk_R r} e^{-pz} \end{aligned} \quad (89)$$

$$\begin{aligned} \psi^G(r, z) = & \left(\frac{j}{2\pi}\right)^{1/2} \frac{1}{\sqrt{k_R r}} \frac{-j(2k_R^2 - k_2^2) (F_y \sin \Theta + F_x \cos \Theta) - 2k_R p F_z}{\mu D'(k_R)/k_R} \\ & \times e^{-jk_R r} e^{-sz} \end{aligned} \quad (90)$$

The displacements of the Rayleigh wave at  $z = 0$  are then

$$\begin{aligned} U_r = & \frac{\partial \varphi}{\partial r} - \frac{\partial \psi}{\partial z} \\ = & \frac{1}{\sqrt{2\pi k_R r}} \left[ \frac{k_R^2(2k_R^2 - k_2^2 - 2sp)}{\mu D'(k_R)} \right] F_z \exp[-j(k_R r - \frac{\pi}{4})] - \frac{1}{\sqrt{2\pi k_R r}} \left[ \frac{k_R k_2^2 s}{\mu D'(k_R)} \right] \\ & \times [F_y \sin \Theta + F_x \cos \Theta] \exp[-j(k_R r + \frac{\pi}{4})] \end{aligned} \quad (91)$$

$$\begin{aligned} U_z = & \frac{\partial \varphi}{\partial z} + \frac{\partial \psi}{\partial r} \\ = & \frac{1}{\sqrt{2\pi k_R r}} \left[ \frac{-k_R k_2^2 p}{\mu D'(k_R)} \right] F_z \exp[-j(k_R r + \frac{\pi}{4})] - \frac{1}{\sqrt{2\pi k_R r}} \left[ \frac{k_R^2(2k_R^2 - k_2^2 - 2sp)}{\mu D'(k_R)} \right] \\ & \times [F_y \sin \Theta + F_x \cos \Theta] \exp[-j(k_R r - \frac{\pi}{4})] \end{aligned} \quad (92)$$

#### B. Stiffness Matrix

Assuming that the forces are uniformly distributed over a disk of radius (b), the displacements at the center are found by convolution. The result is given in terms of the stiffness matrix  $T_{ij}$  (see Appendix D) relating displacements to the forces in Eq. (57).

#### C. Radiation Patterns of the Post Structure

The dynamic equation for the post structure is identical in form to the rail problem [Eq. (59)] except that we ignore the reaction of the scattered wave back on the source. The difficulty in treating the reaction of the scattered wave back on the source is caused by the fact that a detailed energy balance as we have in the rail problem is not as easily carried out. First

of all, the incident wave is a uniform plane wave of infinite extent, while the wave scattered by the point source is more or less radial. Such scattering geometry presents difficulty in the normalization of energy which is not the case in the rail scattering problem. In addition, the effect of the scattered wave on the point source is not as easily treated analytically as for a line source because of the nature of the point singularity. Therefore, it must be kept in mind that our result is an approximation which provides only a qualitative picture of the scattering process.

Assume a uniform Rayleigh wave incident on the post in the x-direction. The induced forces which satisfy the dynamic equation are given by

$$F_x = \frac{-\pi b^2 (1 - \rho_s h \omega^2 T_{11}^U)}{T_{11}^L (1 + T_{11}^U / T_{11}^L - \rho_s h \omega^2 T_{11}^U)} U_x^R \quad (93)$$

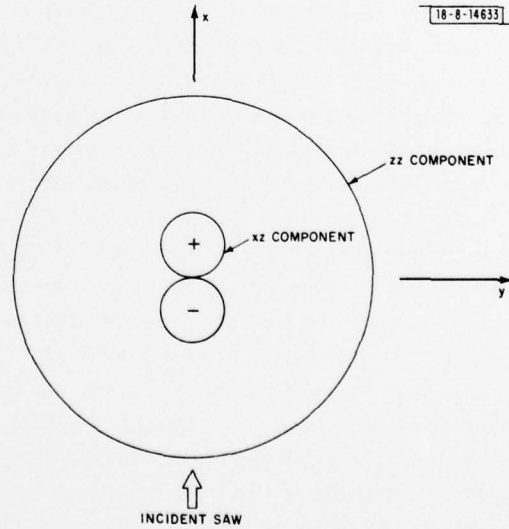
$$F_z = \frac{-\pi b^2 (1 - \rho_s h \omega^2 T_{33}^U)}{T_{33}^L (1 + T_{33}^U / T_{33}^L - \rho_s h \omega^2 T_{33}^U)} U_z^R \quad (94)$$

$$F_y = 0 \quad (95)$$

Substitution into Eqs. (91) and (92) gives the scattered Rayleigh wave.

Note the scattered field decreases as  $1/\sqrt{r}$  from the source as expected for two-dimensional scattering. Furthermore, the radiation pattern of the vertical source component  $F_z$  is isotropic while it has a cosine dependence for the horizontal source component  $F_x$ . The displacement radiation patterns are shown separately in Fig. 15 for a post with a silicon superstrate. It is interesting to note that the scattering in the forward direction is stronger than that in the backward direction because of the constructive interference of the scattered wave components. Furthermore, we observe that the vertically scattered component is larger than the horizontal component. This is because, at the surface, the Rayleigh wave displacement in  $\text{LiNbO}_3$  is 1.5 times

Fig. 15. Displacements of scattered SAW by the post structure.



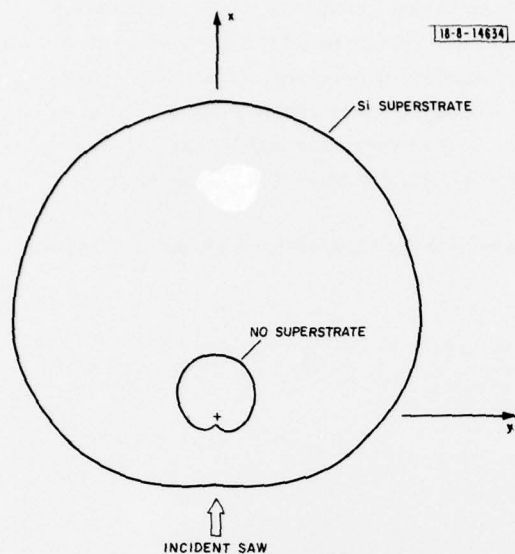


Fig. 16. Radiation pattern of scattered SAW by the post structure.

larger in the vertical direction than in the horizontal direction, inducing a larger  $F_z$  than  $F_x$ . The difference is further enhanced in the excitation of the scattered Rayleigh wave.

The power radiation patterns for a post, with and without superstrate, are shown in Fig. 16. We note that the scattering is dramatically increased by the pinning effect of the superstrates, a phenomenon also observed in the rail scattering.

## VII. SUMMARY

We have presented a model for the scattering of the Rayleigh wave by the rail- and post-support structure. Using the scattering matrix coefficients predicted by our model, we have analyzed the modes in the SAW convolver with a periodic rail structure. The theoretical results obtained are in reasonable agreement with the experimental measurements.<sup>6</sup>

Our study provides insight into the optimal design of the rail support in order to minimize the moding problem. We recommend that the rails be made thinner and placed closer together so as to decrease the ripple size in the output frequency response.

Finally, we recommend further study into the scattering of the Rayleigh wave by rail- and post-support structure by taking the finite dimension of the support structure into account. This would involve a more detailed study of the groove scattering as well as the bulk wave scattering problem.

The groove scattering may very well account for the discrepancy between the theoretically predicted frequency ripple using our present model and the experimental measurement.<sup>6</sup> Furthermore, in order to optimize the rail-structure design and to get a handle on the pressure dependence of the mode pattern, the groove scattering problem must be studied carefully.

Our study has not included loss due to the bulk scattering which is expected to be significant when the deformation caused by the rail loading becomes larger. Furthermore, mode conversion as a result of scattering by nonuniform loading along the rail and scattering by boundary roughness can also contribute to loss. We believe our model is still incomplete without proper account for these loss mechanisms which are important in understanding the limitations on the convolver.

#### ACKNOWLEDGMENTS

The author wishes to express his sincere thanks to Professor H. A. Haus for his encouragements, advice, and many kind discussions which provided the author with a great deal of physical insight into the problem. Experimental evaluation of the device performance by S. A. Reible and his help in editing the final manuscript are greatly appreciated. Many useful discussions with J. H. Cafarella are also acknowledged.

#### REFERENCES

1. W. C. Wang and P. Das, "Surface Wave Convolver via Space Charge Nonlinearity," 1972 Ultrasonics Symposium Proceedings (IEEE, New York, 1972), pp. 316-321.
2. S. A. Reible, J. H. Cafarella, R. W. Ralston, and E. Stern, "Convolver for DPSK Demodulation of Spread Spectrum Signals," 1976 Ultrasonics Symposium Proceedings (IEEE, New York, 1976), pp. 451-455, DDC AD-A040519/1.
3. S. A. Reible, V. S. Dolat, and J. H. Cafarella, "Waveguide Moding in Gap-Coupled Surface Wave Devices," private communication.
4. H. I. Smith, "Techniques for Making Gap-Coupled Acoustoelectric Devices," 1975 Ultrasonics Symposium Proceedings (IEEE, New York, 1975), pp. 238-240, DDC AD-A031719/8.
5. R. Joly, Appl. Phys. Lett. **29**, No. 9 (1 November 1976), pp. 525-527.
6. S. A. Reible, private communication.
7. R. E. Collins, Foundations for Microwave Engineering (McGraw-Hill, New York, 1966).
8. H. A. Haus, "Bulk Scattering Loss of SAW Grating Cascades," IEEE Trans. Sonics Ultrason. **SU-24**, No. 4, 259-267 (July 1977).
9. L. D. Landau and E. M. Lifshitz, Theory of Elasticity (Pergamon Press, London, 1959), p. 29.
10. B. A. Auld, Acoustic Fields and Waves in Solids (Wiley, New York, 1973), Vol. I, p. 357.



APPENDIX A  
GREEN'S FUNCTION OF A MODULATED LINE SOURCE

$$\varphi^G(x, y, z) = \frac{1}{2\pi} \int_{-\infty}^{\infty} dk_x \frac{-(k^2 + s^2) F_z - j2ks(F_x \cos \theta + F_y \sin \theta)}{\mu D(k)} \times e^{-j(k_x x + k_y y)} e^{-pz} \quad (A-1)$$

$$\psi^G(x, y, z) = \frac{j}{2\pi} \int_{-\infty}^{\infty} dk_x \frac{-2kpF_z - j(k^2 + s^2)(F_x \cos \theta + F_y \sin \theta)}{\mu D(k)} \times e^{-j(k_x x + k_y y)} e^{-sz} \quad (A-2)$$

where

$$D(k) = (k^2 + s^2)^2 - 4k^2 ps \quad (A-3)$$

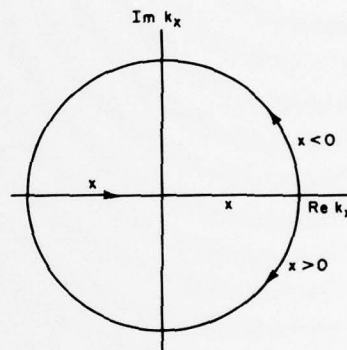
We want to evaluate integrals in Eqs. (B-1) and (B-2) by contour integration in the  $k_x$  complex plane. The only pole singularity occurs at  $k_x = \pm \sqrt{k_R^2 - k_y^2}$ . Letting  $k_R$  be slightly imaginary displaces the poles off the real axis as shown.

For  $x > 0$ , we choose to close the contour in the lower half-plane. To find the residue, we need the derivative of  $D(k)$  evaluated at  $k_x = \sqrt{k_R^2 - k_y^2}$ . This is done by expanding  $D(k)$  in the neighborhood of  $k_x$ :

$$\begin{aligned} D(k) &= (k^2 + s^2)^2 - 4k^2 ps \\ &= (k^2 - k_R^2) R(k) \\ &= (k - k_R)(k + k_R) R(k) \\ &= \left( \sqrt{k_x^2 + k_y^2} - k_R \right) \left( \sqrt{k_x^2 + k_y^2} + k_R \right) R(k) \end{aligned}$$

where  $\sqrt{k_x^2 + k_y^2} + k_R$  and  $R(k)$  are functions with weak dependence on  $k_x$  as  $k_x \rightarrow \sqrt{k_R^2 - k_y^2}$ ; so we can replace the two functions by  $2k_R$  and  $R(k_R)$ , respectively, continue,

$$\begin{aligned} D(k) &\cong \left( \sqrt{k_x^2 + k_y^2} - k_R \right) 2k_R R(k_R) \\ &= \left[ \sqrt{\left( \sqrt{k_R^2 - k_y^2} + \delta \right)^2 + k_y^2} - k_R \right] 2k_R R(k_R) \\ &\cong \left( \sqrt{k_R^2 + 2\delta \sqrt{k_R^2 - k_y^2}} - k_R \right) 2k_R R(k_R) \\ &\cong \frac{\delta \sqrt{k_R^2 - k_y^2}}{k_R} 2k_R R(k_R) \end{aligned}$$



but  $D'(k)|_{k=k_R} = 2k_R R(k_R)$ ; therefore,

$$D' \Big|_{k_x = \sqrt{k_R^2 - k_y^2}} = \frac{D'(k_R) \sqrt{k_R^2 - k_y^2}}{k_R} D'(k_R) \cos \theta \quad . \quad (A-4)$$

Finally, for  $x > 0$ , let  $r = \sqrt{x^2 + y^2}$  to be the distance measured along the  $\gamma$ -axis (see Fig. 8).

$$\varphi^G(r, z) = -j \frac{-(k_R^2 + s^2) F_z - j2k_R s(F_x \cos \theta + F_y \sin \theta)}{\mu D'(k_R) \cos \theta} e^{-jk_R r} e^{-pz} \quad .$$

For  $x < 0$ , we close the contour in the upper half-plane, the result is a change of sign of the  $F_x$  term. A similar contour integration is carried out for  $\psi^G$ . In summary,

$$\varphi^G(r, z) = \frac{-2k_R s(F_y \sin \theta \pm F_x \cos \theta) + j(2k_R^2 - k_2^2) F_z}{\mu D'(k_R) \cos \theta} e^{-jk_R r} e^{-pz} \quad (A-5)$$

$$\psi^G(r, z) = \frac{-j(2k_R^2 - k_2^2) (F_y \sin \theta \pm F_x \cos \theta) - (2k_R p) F_z}{\mu D'(k_R) \cos \theta} e^{-jk_R r} e^{-sz} \quad (A-6)$$

where the plus sign is used for  $x > 0$  and the minus sign for  $x < 0$ .

APPENDIX B  
STIFFNESS TENSOR FOR THE RAIL STRUCTURE

Convolutions are of the form:

$$U_i(x, y) = \int_{-\infty}^{\infty} dy' \int_{-a}^a dx' \frac{1}{2a} U_{ij}^G(x - x', y - y') e^{-jk_y y'} \quad (B-1)$$

where  $U_{ij}^G$  are Green's functions for a point source given by Eqs. (36) to (38) and  $2a$  is the width of the rail. We are only interested in the displacement at the center, i.e.,  $x = 0$ . Integrations of terms with  $U_{ij}^G$  odd in  $x'$  vanish. For the remaining terms we need the following integrals:

$$I_1 = \int_{-\infty}^{\infty} \frac{1}{\rho} e^{-jk_y y'} dy' \quad (B-2)$$

$$I_2 = \int_{-\infty}^{\infty} \frac{1}{\rho^3} e^{-jk_y y'} dy' \quad (B-3)$$

$$I_3 = \int_{-\infty}^{\infty} \frac{(y - y')^2}{\rho^2} e^{-jk_y y'} dy' \quad (B-4)$$

$$I_4 = \int_{-\infty}^{\infty} \frac{(y - y')^2}{\rho^3} e^{-jk_y y'} dy' \quad (B-5)$$

where

$$\rho = \sqrt{x'^2 + (y - y')^2}.$$

Let  $\mu = y' - y$

$$\begin{aligned} I_1 &= e^{-jk_y y} \int_{-\infty}^{\infty} \frac{1}{\sqrt{x'^2 + \mu^2}} e^{-jk_y \mu} d\mu \\ &= e^{-jk_y y} 2 \int_0^{\infty} \frac{\cos k_y \mu}{\sqrt{x'^2 + \mu^2}} d\mu. \end{aligned}$$

Let  $\lambda = \frac{\mu}{x'}$

$$\begin{aligned} I_1 &= e^{-jk_y y} 2 \int_0^{\infty} \frac{\cos(k_y |x'| \lambda)}{\sqrt{1 + \lambda^2}} d\lambda \\ &= e^{-jk_y y} 2 K_0(k_y |x'|) \quad (K_0 \text{ is the modified Bessel function}). \end{aligned}$$

For  $k_y x' \ll 1$ ,

$$I_1 \approx -2 \left( \ln \frac{k_y |x'|}{2} + \zeta \right) e^{-jk_y y} \quad [\text{Eq. (B-2)}]$$

where  $\zeta = 0.57721$ .

Note

$$I_2 = -\frac{1}{x'} \frac{\partial I_1}{\partial x'} = \frac{2}{x'^2} e^{-jk_y y} \quad [\text{Eq. (B-3)}]$$

$$I_3 = e^{-jk_y y} \int_{-\infty}^{\infty} \frac{-\mu}{x'^2 + \mu^2} e^{-jk_y \mu} d\mu$$

$$= j\pi e^{-k_y |x|} e^{-jk_y y} \quad [\text{Eq. (B-4)}]$$

$$I_4 = e^{-jk_y y} \int_{-\infty}^{\infty} \frac{\mu^2}{(x'^2 + \mu^2)^{3/2}} e^{-jk_y \mu} d\mu$$

$$= e^{-jk_y y} \int_{-\infty}^{\infty} \left[ \frac{1}{(x'^2 + \mu^2)^{1/2}} - \frac{x'^2}{(x'^2 + \mu^2)^{3/2}} \right] e^{-jk_y \mu} d\mu$$

$$= [I_1 - x'^2 I_2]$$

$$= -2 \left( \ln \frac{k_y |x'|}{2} + \xi + 1 \right) e^{-jk_y y} \quad [\text{Eq. (B-5)}]$$

Let  $x' \rightarrow 0$ , we note  $I_3$  is well behaved while all other integrals become singular, therefore  $I_3$  can be ignored. Next, the  $x'$ -integrations are done:

$$\int_{-a}^a I_1 dx' = \left( -2 \int_{-a}^a \ln \frac{k_y |x'|}{2} dx' - 4\xi a \right) e^{-jk_y y}$$

$$= 4a \left( 1 - \xi - \ln \frac{k_y a}{2} \right) e^{-jk_y y} \quad (\text{B-6})$$

$$\int_{-a}^a x'^2 I_2 dx' = 4a e^{-jk_y y} \quad (\text{B-7})$$

$$\int_{-a}^a I_4 dx' = -4a \left( \xi + \ln \frac{k_y a}{2} \right) e^{-jk_y y} \quad (\text{B-8})$$

Now, Eq. (B-1) can be put in the form

$$U_i = T_{ij} F_j \quad (\text{B-9})$$

where the stiffness matrix  $T_{ij}$  is diagonal with

$$T_{11} = \frac{2(1+\sigma)}{\pi E} \left[ 1 - (1-\sigma) \left( \xi + \ln \frac{k_y a}{2} \right) \right] \quad (\text{B-10})$$

$$T_{22} = \frac{2(1+\sigma)}{\pi E} \left( 1 - \sigma - \xi - \ln \frac{k_y a}{2} \right) \quad (\text{B-11})$$

$$T_{33} = \frac{2(1+\sigma)}{\pi E} (1-\sigma) \left( 1 - \xi - \ln \frac{k_y a}{2} \right) \quad (\text{B-12})$$



APPENDIX C  
GREEN'S FUNCTION OF A POINT SOURCE

$$\varphi^G(x, y, z) = \frac{1}{(2\pi)^2} \int_{-\infty}^{\infty} dk_y \int_{-\infty}^{\infty} dk_x \frac{-(k^2 + s^2) F_z - j2ks(F_x \cos \theta + F_y \sin \theta)}{\mu D(k)} \times e^{-j(k_x x + k_y y)} e^{-pz} \quad (C-1)$$

$$\psi^G(x, y, z) = \frac{1}{(2\pi)^2} \int_{-\infty}^{\infty} dk_y \int_{-\infty}^{\infty} dk_x \frac{-2kpF_z - j(k^2 + s^2)(F_x \cos \theta + F_y \sin \theta)}{\mu D(k)} \times e^{-j(k_x x + k_y y)} e^{-sz} \quad (C-2)$$

Evaluating the  $k_x$  integration as done in Appendix A gives

$$\varphi^G(x, y, z) = \frac{1}{2\pi} \int_{-\infty}^{\infty} dk_y \frac{-2k_R s(F_y \sin \theta + F_x \cos \theta) + j(2k_R^2 - k_y^2) F_z}{\mu D'(k_R) \frac{\sqrt{k_R^2 - k_y^2}}{k_R}} \times \exp \left[ -j(k_y y + \sqrt{k_R^2 - k_y^2} x) \right] e^{-pz} \quad (C-3)$$

$$\psi^G(x, y, z) = \frac{1}{2\pi} \int_{-\infty}^{\infty} dk_y \frac{-j(2k_R^2 - k_y^2)(F_y \sin \theta + F_x \cos \theta) - 2k_R p F_z}{\mu D'(k_R) \frac{\sqrt{k_R^2 - k_y^2}}{k_R}} \times \exp \left[ -j(k_y y + \sqrt{k_R^2 - k_y^2} x) \right] e^{-sz} \quad (C-4)$$

Integrations in  $k_y$  are done by the steepest descent method. Evaluate  $\varphi^G$  first:

$$\varphi^G(x, y, z) = \frac{1}{2\pi} \int_{-\infty}^{\infty} dk_y F(k_y) \exp \left[ -j(k_y y + \sqrt{k_R^2 - k_y^2} x) \right] e^{-pz}$$

Let the saddle point be  $(k_{x'}, k_{y'})$  then

$$\frac{\partial}{\partial k_y} (k_y y + \sqrt{k_R^2 - k_y^2} x) \Big|_{k_{y'}} = 0 \quad ; \quad y - x \frac{k_{y'}}{\sqrt{k_R^2 - k_{y'}^2}} = 0 \quad ; \quad \frac{y}{x} = \frac{k_{y'}}{k_{x'}}$$

$$\frac{\partial^2}{\partial k_y^2} (k_y y + \sqrt{k_R^2 - k_y^2} x) \Big|_{k_{y'}} = -x \frac{k_R^2}{k_{x'}^3}$$

$$\varphi^G(x, y, z) = \frac{1}{2\pi} F(k_{y'}) e^{-j(k_{y'} y + k_{x'} x)} \int_{S.D.} d\Delta k_y \exp \left[ j \frac{1}{2} x \frac{k_R^2}{k_{x'}^3} (\Delta k_y)^2 \right] \quad (C-5)$$

Steepest decent path (S.D.) is

$$\Delta k_y = j^{1/2} \mu$$

$$d\Delta k = j^{1/2} d\mu$$

$$\int_{S.D.} \rightarrow j^{1/2} \int_{-\infty}^{\infty} d\mu \frac{-\mu^2}{2\sigma^2} = j^{1/2} \sqrt{2\pi\sigma^2}$$

where

$$\sigma^2 = \frac{k_{x'}^3}{x k_R^2}$$

$$\varphi^G(x, y, z) = \frac{1}{2\pi} F(k_{y'}) e^{-j(k_{y'} y + k_{x'} x)} j^{1/2} \sqrt{2\pi\sigma^2}$$

Thus,

$$\begin{aligned} \varphi^G(r, z) &= \left(\frac{j}{2\pi}\right)^{1/2} \frac{1}{\sqrt{k_R r}} \frac{-2k_R^2 (F_y \sin \theta + F_x \cos \theta) + j(2k_R^2 - k_2^2) F_z}{\mu D'(k_R)/k_R} \\ &\times e^{-jk_R r} e^{-pz} \end{aligned} \quad (C-6)$$

Similarly,

$$\begin{aligned} \psi^G(r, z) &= \left(\frac{j}{2\pi}\right)^{1/2} \frac{1}{\sqrt{k_R r}} \frac{-j(2k_R^2 - k_2^2) (F_y \sin \theta + F_x \cos \theta) - 2k_R^2 p F_z}{\mu D'(k_R)/k_R} \\ &\times e^{-jk_R r} e^{-sz} \end{aligned} \quad (C-7)$$

where

$$r = \sqrt{x^2 + y^2}$$

APPENDIX D  
STIFFNESS TENSOR FOR THE POST STRUCTURE

Convolutions are of the form:

$$U_i = \int_0^b \frac{U_{ij}^G(\bar{r} - \bar{r}')}{\pi b^2} 2\pi r' dr' \quad . \quad (D-1)$$

Note

$$I_4 = \int_0^{2\pi} \int_0^b \frac{x^2}{r^3} r' dr' d\theta = \pi b \quad (D-2)$$

then (D-1) can be put in the form:

$$U_i = T_{ij} F_j \quad (D-3)$$

where the stiffness matrix  $T_{ij}$  is diagonal with

$$T_{11} = T_{22} = \frac{(2 + \sigma - \sigma^2) b}{E} \quad (D-4)$$

$$T_{33} = \frac{2(1 - \sigma^2) b}{E} \quad . \quad (D-5)$$

UNCLASSIFIED

SECURITY CLASSIFICATION OF THIS PAGE (When Data Entered)

REPORT DOCUMENTATION PAGE		READ INSTRUCTIONS BEFORE COMPLETING FORM
1. REPORT NUMBER ESD-TR-78-3 ✓	2. GOVT ACCESSION NO.	3. RECIPIENT'S CATALOG NUMBER
4. TITLE (and Subtitle)  Modal Analysis of SAW Convolver		5. TYPE OF REPORT & PERIOD COVERED  Technical Report
		6. PERFORMING ORG. REPORT NUMBER  Technical Report 526 ✓
7. AUTHOR(s)  Karl L. Wang, Consultant		8. CONTRACT OR GRANT NUMBER(s)  F19628-78-C-0002 ✓
9. PERFORMING ORGANIZATION NAME AND ADDRESS Lincoln Laboratory, M. I. T. P. O. Box 73 Lexington, MA 02173		10. PROGRAM ELEMENT, PROJECT, TASK AREA & WORK UNIT NUMBERS ARPA Order 2929 Program Element No. 62708E Project No. 8T10
11. CONTROLLING OFFICE NAME AND ADDRESS Defense Advanced Research Projects Agency 1400 Wilson Boulevard Arlington, VA 22209		12. REPORT DATE  13 January 1978
		13. NUMBER OF PAGES  40
14. MONITORING AGENCY NAME & ADDRESS (if different from Controlling Office)  Electronic Systems Division Hanscom AFB Bedford, MA 01731		15. SECURITY CLASS. (of this report)  Unclassified
		15a. DECLASSIFICATION DOWNGRADING SCHEDULE
16. DISTRIBUTION STATEMENT (of this Report)  Approved for public release; distribution unlimited.		
17. DISTRIBUTION STATEMENT (of the abstract entered in Block 20, if different from Report)		
18. SUPPLEMENTARY NOTES  None		
19. KEY WORDS (Continue on reverse side if necessary and identify by block number)		
SAW acoustoelectric convolver	acoustic waveguide gap-coupled convolver	Rayleigh wave surface wave modes mode analysis
20. ABSTRACT (Continue on reverse side if necessary and identify by block number)		
<p>The gap-coupled acoustoelectric convolver developed at Lincoln Laboratory is a surface-acoustic-wave (SAW) device consisting of a LiNbO<sub>3</sub> delay line and a silicon strip supported on a series of spacer rails (or posts) which have been ion-beam etched into the LiNbO<sub>3</sub> surface. The silicon/air-gap/LiNbO<sub>3</sub> structure forms an over-moded acoustic waveguide. A theoretical model has been developed which analyzes the perturbing effect of rails and predicts the mode structure and beating phenomena between modes. The scattering by support posts is also analyzed.</p>		

DD FORM 1473  
1 JAN 73

EDITION OF 1 NOV 65 IS OBSOLETE

UNCLASSIFIED

SECURITY CLASSIFICATION OF THIS PAGE (When Data Entered)